Welding in the World (2023) 67:51–62
https://doi.org/10.1007/s40194-022-01398-y

RESEARCH PAPER

Grain growth and precipitation behaviour of AISI 430 ferritic stainless steel subjected to pulsed laser beam welding using free-form pulse shaping

N. Sommer[1] · F. Stredak[1] · M. Wiegand[1] · S. Böhm[1]

Received: 3 August 2022 / Accepted: 11 October 2022 / Published online: 26 October 2022

Abstract
Ferritic stainless steels are prone to grain coarsening and precipitation of chromium-rich grain boundary phases during fusion welding, which increase intergranular corrosion susceptibility. State-of-the-art techniques to overcome these challenges mainly feature heterogeneous nucleating agents with regard to grain coarsening or alternating alloy concepts as well as post-weld heat treatments as for restoration of intergranular corrosion resistance. The present investigation seeks to depart from these traditional approaches through the use of a tailored heat input during pulsed laser beam welding by means of free-form pulse shaping. Grain size analysis using electron backscatter diffraction shows a substantial reduction of grain size as compared to continuous-wave lasers due to a distinctive columnar to equiaxed transition. Moreover, phase analyses reveal the overcoming of chromium carbide precipitation within the heat-affected zone. As corrosion tests demonstrate, intergranular attack is therefore concentrated on the weld metal. In comparison to continuous-wave laser beam welding, intergranular corrosion susceptibility is substantially reduced for very short pulse durations. From these results, it can be derived that pulsed laser beam welding using free-form pulse shaping enables direct control of heat input and, thus, tailored grain growth and precipitation formation properties.

Keywords Ferritic stainless steel · Pulsed laser beam welding · Intergranular corrosion · Grain coarsening · Grain refinement · Precipitation kinetics

1 Introduction and state-of-the-art

Ferritic stainless steels (FSS) exhibit excellent resistance to stress corrosion cracking [1] as well as high-temperature oxidization [2] and offer very good workability and formability with limited springback [3]. As a result, they are considered to be a suitable substitution for austenitic stainless steels (ASS) [3, 4], e.g. in hot natural water, which has promoted the use of FSS in manifold applications such as household appliances [5]. In contrast, the substantial omission of nickel in the alloying concept also enables the solidification of FSS in the body-centred-cubic (bcc) lattice, which results in rapid diffusion velocities and low solubility for interstitial elements, such as carbon or nitrogen [6]. These rapid diffusion velocities promote both, the precipitation of carbides and nitrides, as well as grain coarsening at elevated temperatures [6, 7]. Notably, the diffusion-induced precipitation of chromium-rich grain boundary phases represents an ongoing challenge and may either be initiated during solid-state heat treatments [8, 9] or the thermal cycle during welding [10]. This leads to a localized reduction of chromium content around these precipitates, so-called chromium depletion, for which the protective passive layer cannot form and corrosive attack along the depleted regions is rendered possible [11]. This particular form of selective corrosion is referred to as intergranular corrosion (IGC) and may propagate along such sensitized grain boundaries which leads to catastrophic failure of welded joints [12]. Moreover, the weld metal (WM) of FSS is prone to substantial grain coarsening in dependence on the temperature gradient G and

Recommended for publication by Commission IV - Power Beam Processes

✉ N. Sommer
n.sommer@uni-kassel.de

[1] Department for Cutting and Joining Manufacturing Processes, Institute of Production Technology and Logistics, University of Kassel, Kurt-Wolters-Straße 3, 34125 Kassel, Germany

solidification rate R present within the melt [13, 14]. On the one hand, grain coarsening reduces the ductility of the joint [15] and, on the other hand, further promotes the susceptibility to IGC [16]. Despite its steep temperature gradients and rapid solidification due to a small melt pool size resulting from comparatively high welding speeds [17], laser welding also using state-of-the-art continuous-wave disk or fibre lasers has proved ineffective to eliminate the aforementioned phenomena [18, 19].

As a result, a multitude of approaches have been developed to combat the two phenomena. Firstly, a post-weld heat treatment (PWHT) can enable the back-diffusion of chromium into depleted regions [20] or, following solution annealing, prevent the precipitation of chromium-rich grain boundary phases [21]. However, the aforementioned techniques may not be carried out on large components due to size limitations and are associated with increased production costs [12]. Secondly, the carbon and nitrogen contents may be set below the solubility limit of the respective grade, for which the precipitation of carbides and nitrides is prevented. Such extra low interstitials (ELI) are immune to IGC after welding [22], but the required purity levels are a challenge to alloy design and, thus, cost-intensive [23]. Moreover, the effects of grain coarsening during welding are amplified [24]. Furthermore, so-called stabilization may be undertaken to increase the IGC resistance of FSS [25]. It comprises the addition of titanium, niobium or zirconium, which feature a higher affinity for carbon than chromium, to form preferential precipitates and, as such, omit chromium depletion [26]. However, recent findings with respect to solid-state heat treatments indicate that unreacted chromium can segregate around these precipitates for which IGC is enabled again [27–29]. Moreover, titanium inclusions may initiate other selective corrosion phenomena such as pitting corrosion [30, 31]. In addition, WM grain boundaries occupied by titanium precipitates are prone to dissolution and, thus, the initiation of special forms of IGC which impair the structural integrity of the component [31]. Recent investigations also demonstrate the use of powder-fed laser cladding [32] in order to locally improve the IGC resistance of ferritic stainless steel welds [33].

In order to alleviate grain coarsening in ferritic stainless welds, a number of studies detail the use of heterogeneous nucleating agents, such as titanium nitride, e.g. in gas tungsten arc welding (GTAW) [34] or laser-based powder-bed-fusion (PBF-LB) [35]. Other studies report on the superimposition of ultrasound by ultrasonically excited filler material, which results in grain refinement within the WM [36]. As the solidification rate and temperature gradient within the melt pool pose the greatest influence on the solidification structure [37], Reddy and Mohandas employ a pulsating arc and, thus, obtain a manipulated melt pool convection which results in dendrite fragmentation and grain refinement [38]. Based on these findings, the so-called metallurgical pulse shaping was developed for pulsed laser beam welding (P-LBW), which enables the precise tailoring of heat input as well as a maximized nucleation rate through melt undercooling [39]. The free-form sequencing of the laser pulse and oscillation of laser power results in a melt pool oscillation [40] and, thus, substantial grain refinement in ASS as well as aluminium and titanium [39].

The present investigation seeks to depart from conventional measures to combat the phenomena of grain coarsening and sensitization in FSS through the use of P-LBW with free-form pulse shaping and, thus, tailored heat input. While previous publications detail the use of P-LBW to joint FSS [41, 42], they lack the fundamental investigation of process-property interrelationships in terms of solidification structure and precipitation behaviour. Therefore, the authors of the investigation at hand employ a free-form pulse shape during P-LBW in order to study the effects on grain refinement and overcome the inherent precipitation of chromium-rich grain boundary phases to mitigate IGC susceptibility.

2 Materials and methods

2.1 Stainless steel and welding procedure

AISI 430 ferritic stainless steel sheet with approximate dimensions of $50 \times 15 \times 0.8$ mm^3 in cold-rolled and blank-annealed surface condition was used for the welding experiments. The chemical composition of the sheet is depicted in Table 1.

The experiments were performed as bead-on-plate weldments with a pulsed, lamp-pumped Nd:YAG laser (LASAG SLS200 CL8, ROFIN LASAG AG, Switzerland) featuring a near-Gaussian intensity distribution and were carried out without filler material. The beam was guided to the workpiece using a step-index fibre with a diameter of 50 µm. The use of a collimation lens with a focal length of 150 mm and focussing optics with a focal length of 100 mm

Table 1 Chemical composition of AISI 430 sheet material, partially adopted from [19] under CC-BY-4.0-license and supplemented

Element (wt.-%)										
Fe	C	N	Cr	Ti	Ni	Mo	Si	Mn	P	S
bal	0.041	0.142	16.18	0.001	0.156	0.046	0.241	0.549	0.040	< 0.001

yielded an approximate beam diameter of 33 µm on the workpiece. Argon shielding gas (purity > 99.998%) was used to protect the seam root and bead top. Weldments were fabricated using a traverse speed of 15 mm/min and a pulse frequency of 5 Hz. In order to obtain a metallurgical pulse shape [39], the laser pulse was sequenced into three sections as depicted in Fig. 1. In the first sequence, the formation of the keyhole takes place with maximum laser power. Subsequently, the laser power is reduced to prevent melt pool overheating and oscillates in order to obtain defined melt undercooling conditions. Lastly, the laser power is continuously reduced to zero and, thus, the melt solidifies [39]. All weldments were performed with a peak power of 500 W and varying pulse lengths of 1 ms, 3 ms and 5 ms and yielding pulse energy inputs of 226.94 mJ, 680.82 mJ and 1134.71 mJ, respectively. These were calculated on basis of the integrated laser power along the time axis of the metallurgical pulse shape.

2.2 Specimen characterization

Following the welding experiments, the specimens were embedded in cold-curing epoxy resin, mechanically ground to grit size P2500 using silicone-carbide paper and polished to 0.1 µm surface finish using colloidal silicone dioxide solution. Subsequently, the cross-sections were etched using V2A-etchant and inspected by means of optical microscopy (OM, Leica DM2700).

For grain size and phase analysis, the specimens were mechanically ground to grit size P2500 and polished using colloidal diamond solution (grit size 0.05 µm). Electron backscatter diffraction (EBSD) was carried out using a scanning electron microscopy (SEM, Zeiss REM Ultra Plus) operated at an acceleration voltage of 20 kV using a CCD-based EBSD detector (Bruker e-flash). Overviews with a magnification of 100 × were obtained using a pixel size of 1 µm in order to allow for precise grain size analysis. The precipitation behaviour was analyzed using a magnification of 2500 × and a pixel size of 40 nm. Post-process analysis was carried out using ATEX software (version 3.26) [43].

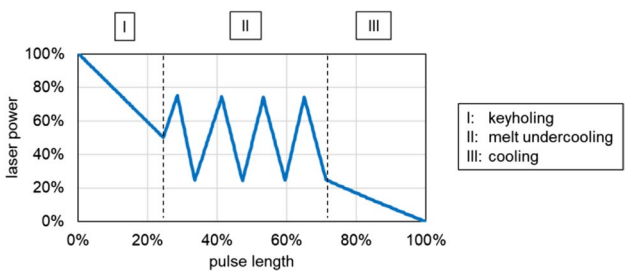

Fig. 1 Schematic depicting the metallurgical pulse shape employed during the P-LBW experiments

To visualize grain boundary precipitates, the samples were briefly treated with V2A-etchant and inspected with the in-lens, energy-selective backscatter detector (ESB) using the SEM mentioned beforehand operated at an acceleration voltage of 3 kV.

Corrosion tests were carried out on basis of the Strauß test in DIN EN ISO 3651–2 [44]. Prior to the corrosion tests, the samples were brushed with a stainless steel brush in order to remove any dirt of the surface. Subsequently, the samples were rinsed with isopropanol and air-dried. The samples were then contacted with copper chips on the bottom of a glass flask and immersed in a solution of 138 g sulphuric acid ($\rho_{20} = 1.84$ g/L) and 75 g copper-sulphate penta-hydrate dissolved in desalinated water. The thus obtained total solution volume of 750 mL was brought to boiling temperature using an oil bath. Corrosion tests were undertaken with distinctive immersion durations of 10 h, 20 h and 40 h. The mass loss of the samples was measured with a high-accuracy weighing machine (KERN ABT 120-5DM). In order to mitigate statistical errors, three individual samples were measured for each immersion duration and set of welding parameters.

3 Results and discussion

3.1 Microstructure and grain size analysis

The AISI 430 weld macrostructure features distinctively different characteristics for varying pulse durations, as Fig. 2 visualizes. An increase of pulse duration yields substantially enlarged WM cross-section areas. As can be derived from the etched micrographs in Fig. 2b d, these enlarged WM cross-sections can be attributed to a wider weld seam and deeper sheet penetration.

Based on the extended dwell time of the laser pulse, it can be deduced that both, the existence of the keyhole and heat conduction to adjacent regions, are prolonged with an increase in pulse duration. This can be seen in good agreement to results published by Xue et al. [45] on P-LBW of DP1000 steel. Also, it has to be noted that some cross-sections feature spherical pores which may result from the collapse of the keyhole and an entrapment of shielding gas within the melt [46].

EBSD analyses of the cross-sections using superimposed image-quality mapping (IQM) and inverse-pole-figure mapping (IPFM) in Fig. 3 reveal that the WM microstructure is characterized by negligible texturing regardless of the pulse duration employed. A detailed analysis of the WM and heat-affected zone (HAZ) transition shows larger grains within the WM than in the HAZ. In the latter, an increased number of grains with nearly equiaxed morphology can be seen. For all given pulse durations, this feature ensures a

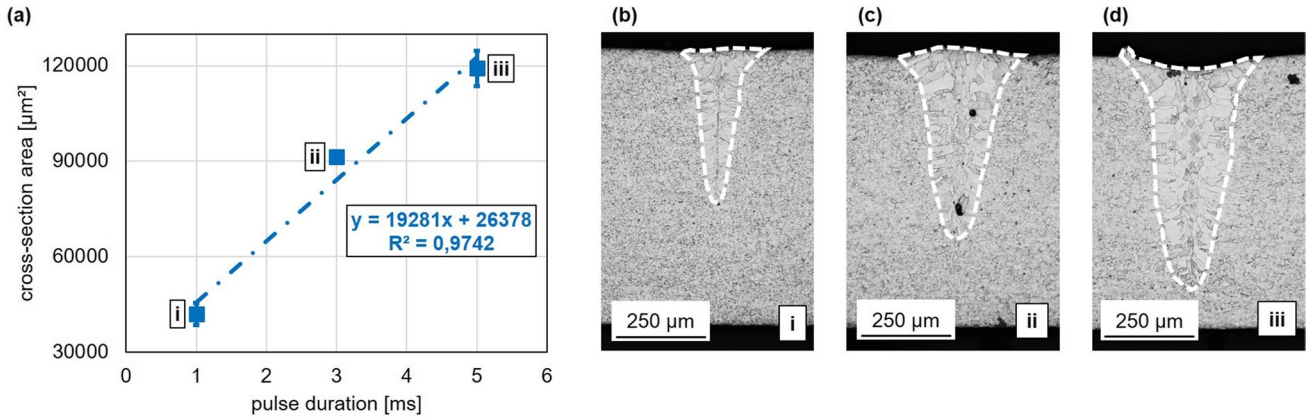

Fig. 2 (a) Mean values of AISI 430 FSS weld metal cross-section area following P-LBW with alternating pulse durations. Mean values computed from three independent experiments; error bars show standard deviation. Best-fit curve represents a linear function with shown parameters and coefficient of determination R^2. (b), (c) and (d) depict etched cross-sections to visualize the weld macrostructure at a given pulse duration

clear identification of the fusion line. In contrast, grains in the immediate vicinity of the fusion line and within the WM are elongated towards the weld centre and occasionally reach lengths which are a multiple of the ones found within the HAZ. As can be derived from the combined IQM and phase mappings (PM), the microstructure within the transition region of all specimens is primarily ferritic with a bcc lattice. However, some face-centred-cubic (fcc) austenite is formed at WM grain boundaries. Typically, residual austenite of FSS is transformed to martensite upon cooling during the welding cycle [47]. As Pekkarinen and Kujanpää [48] suggest based on their investigation on the influence of heat input during continuous-wave laser beam welding (cw-LBW) of AISI 430, the formation of martensite may be suppressed if the cooling rate is high enough to prevent the ferrite–austenite transformation. While EBSD analysis can precisely distinguish fcc-austenite within a bcc-ferrite matrix, the differentiation of bcc-ferrite and body-centred-tetragonal martensite may be complex and insufficient due to an almost identical lattice parameter [49].

However, the distinction of martensite in a bcc-matrix is feasible during EBSD analysis through its alternating morphology [50]. Consequently, the only microstructural features which may be identified as martensite are visible within the WM of a specimen welded at a pulse duration of 5 ms (cf. Figure 3c. The formation at grain boundaries within the WM is in good agreement to previous reports on LBW of FSS by Taban et al. [47]. In consideration of results on the interrelationships of pulse duration and WM cross-section area shown in Fig. 2, it appears plausible that the specimen welded with a pulse duration of 5 ms opened a sufficiently large enough timeframe for ferrite–austenite transformation to occur. On the contrary, the absence of martensite in the WM of specimens welded at pulse durations of 1 ms and 3 ms in combination with the detection of retained fcc-austenite phases in all specimens regardless of the pulse duration cannot be readily explained. Given the pronounced cooling rate during P-LBW, a martensitic transformation is to be anticipated. Yet, recent findings of Chan et al. [51], who report on laser-surface melting of AISI 430, support the observations that some retained austenite is distinguishable in the fusion zone of melted and solidified AISI 430, in particular at grain boundaries. Presumably, the continuance of austenite in the WM may be aided by local impurities or segregations, which halt the transformation process, e.g. as reported on in titanium [52]. Nevertheless, this theory can only be confirmed by an in-depth analysis of the chemical composition, for instance by energy-dispersive X-ray spectroscopy, and, thus, shall not be discussed further within the scope of the investigation at hand.

The grain size investigation, on the other hand, reveals two distinctive regions regardless of the pulse duration employed, as Fig. 4a-c visualize.

From the fusion line, a columnar region facing the weld centre is established. These grains grow perpendicular to the melt pool boundary and, consequently, the temperature gradient G, which is steepest in these regions due to the incumbent heat flow direction [14]. As can be derived from the colour-coded images (cf. Figure 4a-c), these grains exhibit substantially larger sizes than within the base material. Furthermore, the grain size in this region is increased with prolonged pulse durations. Obviously, extended pulse durations lead to larger melt pool dimensions as a result of increased energy input. Therefore, a longer time is required for complete heat dissipation and, thus, the grains are subjected to the boundary conditions of columnar growth for a longer time. Simultaneously, the increased energy input may favour the overall growth of larger grains. This can be

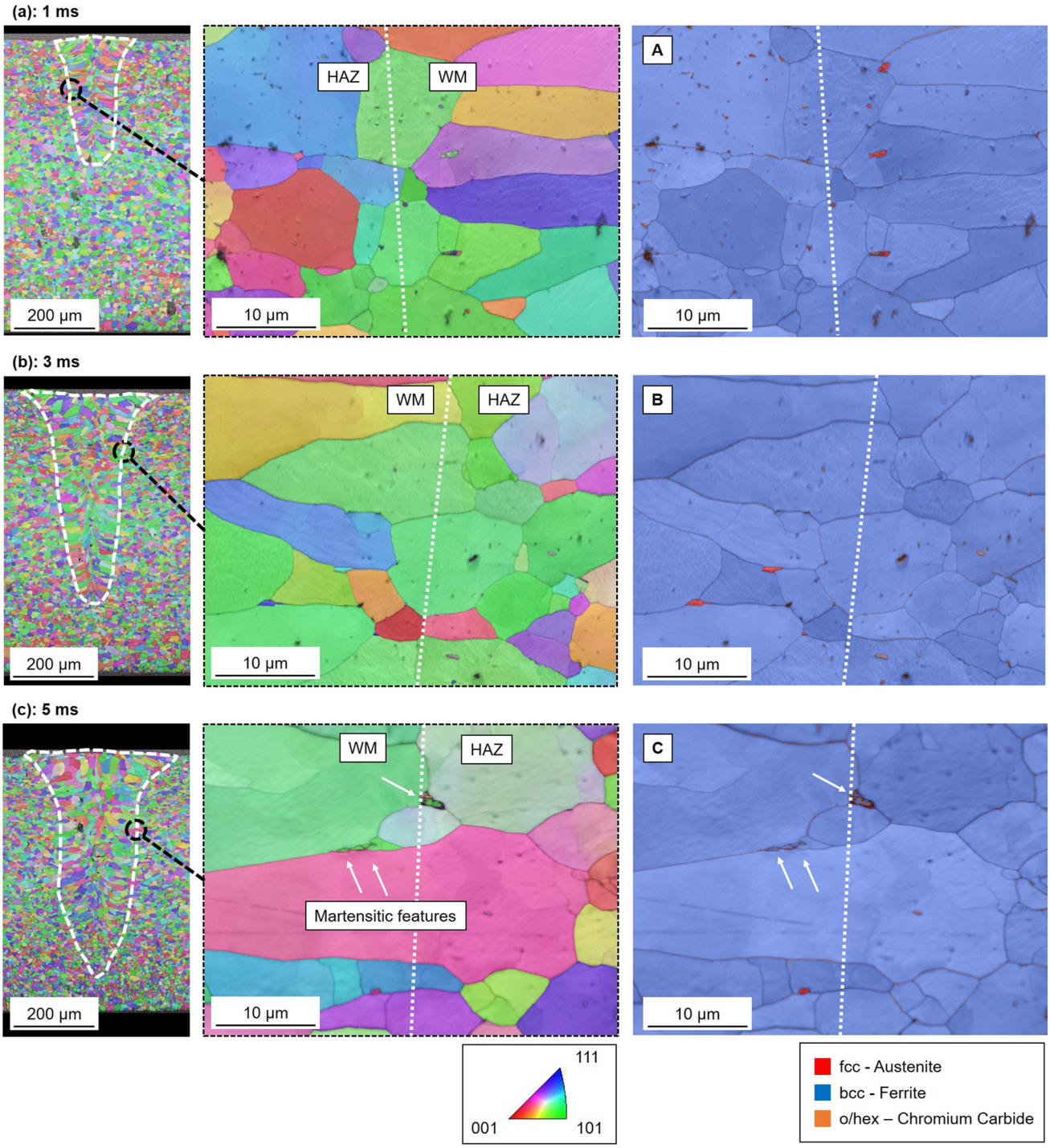

Fig. 3 EBSD overviews and detailed EBSD analyses of the WM/HAZ transition of P-LBW AISI 430 with pulse durations of (a) 1 ms, (b) 3 ms and (c) 5 ms. The left column represents the combined IQM/IPFM overviews of each parameter while the middle column shows the detailed IQM/IPFM of the WM/HAZ transition. Grain orientations plotted perpendicular to traverse direction. The right column depicts the combined IQM/PM of the transition region; dashed line visualizes the fusion line. Designation A to C for detailed phase analysis in Fig. 5

verified by the quantitative grain size analysis in Fig. 4d, which visualizes an exponential growth of the WM grain size with increasing pulse duration and is in good agreement to results presented by Wilden et al. [39]. Hence, it is appropriate to conclude that a comparatively long pulse duration with its relatively high heat and energy input yields

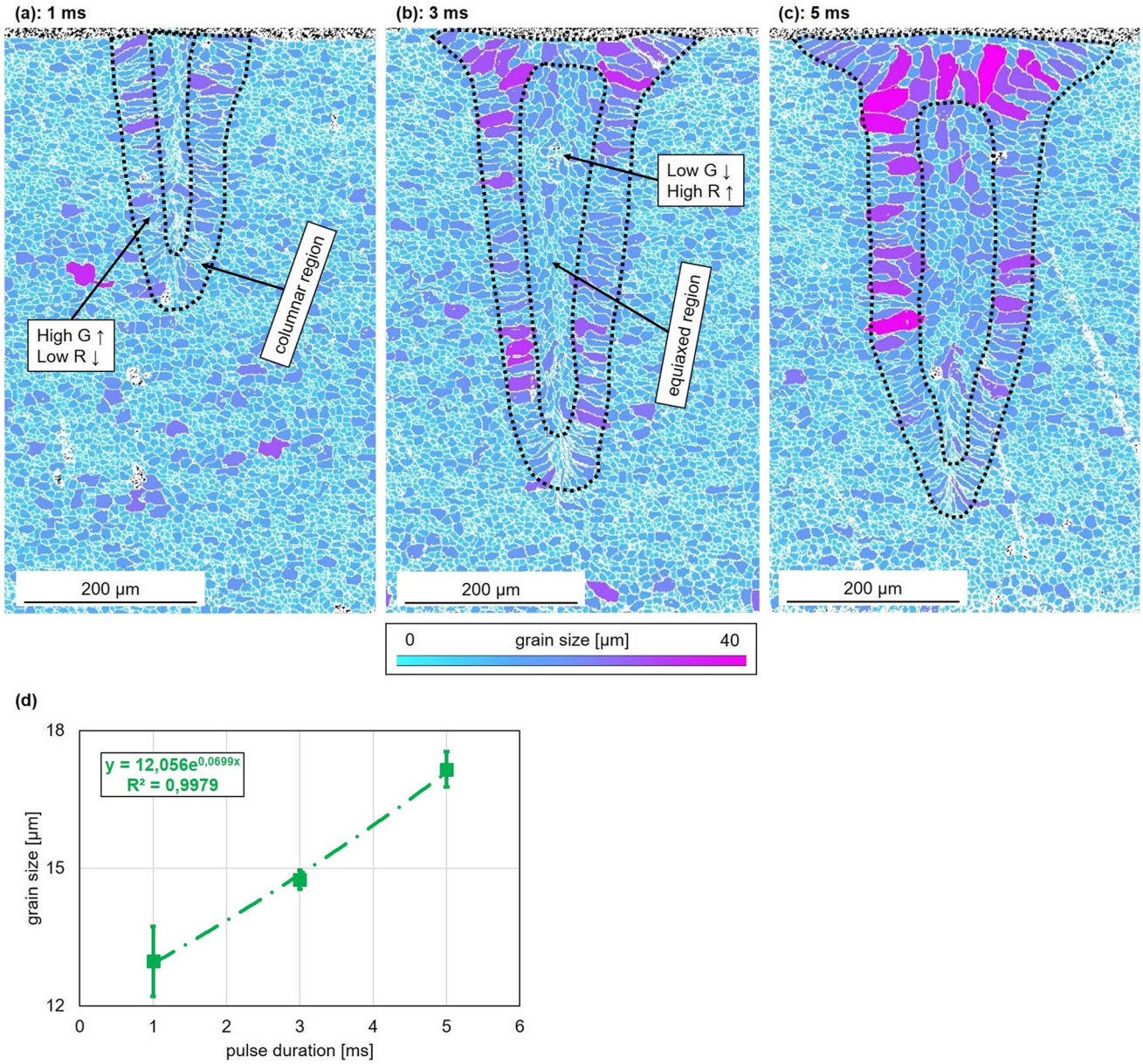

Fig. 4 (a)–(c) Analysis of the grain size evolution at alternating pulse durations demonstrating the columnar to equiaxed transition. Dashed lines represent interfaces of distinctive microstructural features. (d) Quantitative grain size analysis within the weld metal using ATEX [43]. Mean values calculated from three individual measurements; error bars represent standard deviation. Best-fit curve depicts an exponential function with given parameters and coefficient of determination R^2. Grain size of base material is 8.75 µm, computed mean value of nine individual measurements

an enlarged window for diffusion processes to take place. Accordingly, diffusion processes are somewhat limited at pulse durations of 1 ms.

Within the weld centre, the grains exhibit an equiaxed morphology. In this region, the temperature gradient is reduced while the solidification rate is increased. Notably, the equiaxed region is separated from the weld bead surface by another columnar region when a pulse duration of 5 ms is employed. The directional growth of grains towards the bead surface indicates pronounced heat dissipation during the late stages of solidification, which proceeds upward from the weld root to its surface. For all investigated pulse durations, the grain size within the equiaxed region is comparable to the grain size of the base material. In light of previous investigations on P-LBW of FSS [41, 42], it is evident that the use of a free-form pulse shape enables a pronounced columnar to equiaxed transition within the melt metal microstructure. In consideration of earlier reports on the effects of

metallurgical pulse shaping on other alloys [39], it can be deduced that the columnar to equiaxed transition identified in the present investigation can be attributed to increased melt pool convection and inherent dendrite fragmentation, which leads to grain refinement.

Furthermore, the results demonstrate that the cross-section area of the equiaxed region is enlarged with increasing pulse durations. Based on the rising cross-section area of the WM (cf. Figure 2), this feature appears plausible and, simultaneously, confirms the successful imposition of increased melt pool convection as well as dendrite fragmentation regardless of the pulse duration employed due to free-form pulse shaping.

3.2 Precipitation kinetics and intergranular corrosion behaviour

The use of EBSD-based phase mappings at a high magnification facilitates a robust and prompt means to characterize chromium carbide precipitates at the WM/HAZ boundary [33], whose dimensions following cw-LBW typically lie in the order of tenths to hundreds of nanometres [31]. The crystallographic investigation in Fig. 5 visualizes two alternating morphologies and locations of chromium carbides.

Firstly, intragranular chromium carbides can be detected within the HAZ of samples welded at pulse durations of 1 ms and 3 ms. The size of these precipitates matches the size of chromium carbides within the base material of AISI 430 in good approximation [19]. Secondly, the PM of a specimen welded with a pulse duration of 1 ms reveals that grain boundaries in close proximity to the fusion line are occupied by a thin sequence of chromium carbides. Moreover, continuous networks of intergranular chromium carbide precipitates can be identified at grain boundaries within the WM and at the fusion line grain boundaries for pulse durations of 3 ms and 5 ms (cf. Fig. 5b, c). For all investigated samples, the occupation density of grain boundaries with chromium carbides varies strongly with location and pulse duration. When comparing the grain boundary phase precipitation morphology at pulse durations of 1 ms and 5 ms, it can be derived that the lateral extension of chromium phase precipitation along grain boundaries is enlarged for the sample welded with a pulse duration of 5 ms. In consideration of the increased heat input as a result of prolonged pulse duration, it can be derived that the increased lateral extent is to be attributed to extended diffusion conditions. Furthermore, it has to be noted that grain boundary chromium carbides also precipitate adjacent to intragranular chromium carbides in the HAZ of a specimen welded with a pulse duration of 3 ms (see detail on right hand side in Fig. 5b). In consideration of the precipitate size, it is to be inferred that this specific precipitate did not emerge during the thermal cycle of the welding process, but has rather existed beforehand. Consequently, the grain boundary chromium carbides can only have been formed through diffusion of chromium in the immediate vicinity of the grain boundary. This emphasizes the desired diffusion limitation through rapid cooling rates during P-LBW.

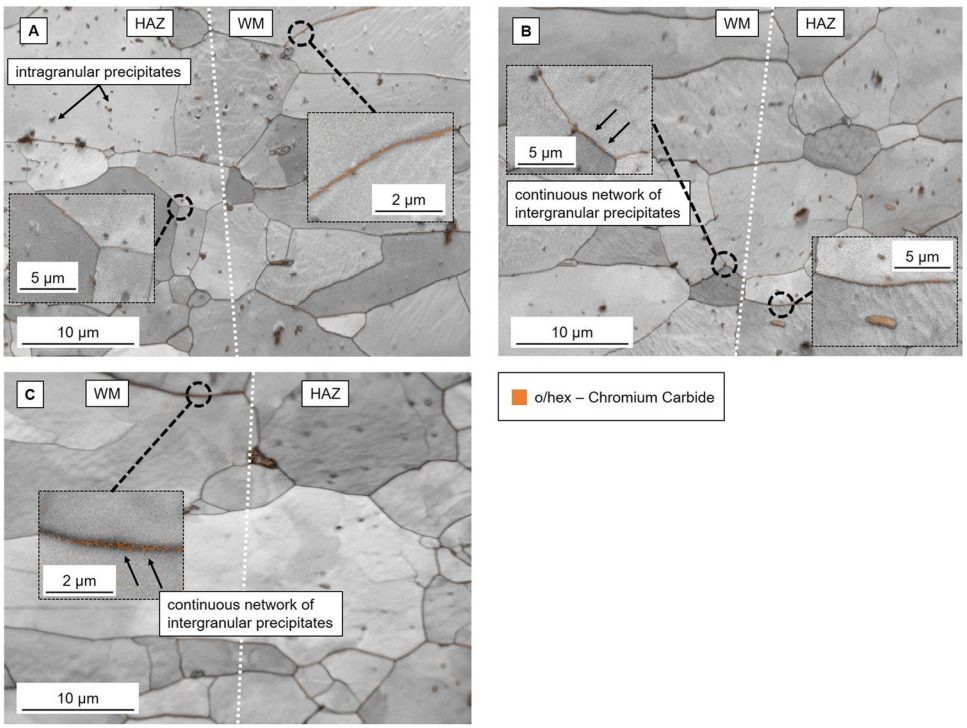

Fig. 5 Analysis of orthorhombic and hexagonal chromium carbide precipitation at the WM/HAZ transition using combined QM/PM. Designation A to C according to Fig. 3

With regard to the occupation density of WM grain boundaries with chromium carbides and their lateral extent, the ESB images in Fig. 6 shed light on the alternating precipitation kinetics as a result of varying pulse duration.

Accumulations of chromium are visible as dark spots due to their lower atomic number in contrast to the surrounding matrix. At a given pulse duration of 1 ms, the chromium precipitates segregate at grain boundaries. However, in between the grain boundary precipitates, clear discontinuities are visible (cf. Fig. 6a). In contrast, the chromium precipitates at a pulse duration of 5 ms (cf. Fig. 6b) form a continuous network and are of larger size than the aforementioned (please note alternating scale bar). Analogue to the grain size analysis, it is thus appropriate to conclude that a pulse duration of 5 ms yields a substantially higher heat input as opposed to 1 ms, for which the boundary conditions for chromium diffusion and carbide precipitation are favourable over a prolonged timespan. In consideration of the interdependencies of chromium carbide precipitation and IGC resistance, it is to be expected that the IGC resistance of specimens welded with a pulse duration of 1 ms is superior to the one of longer pulse durations.

This theory is supported by etched micrographs obtained following corrosion testing and depicted in Fig. 7.

After an immersion duration of 10 h, the specimen welded with a pulse duration of 1 ms does not indicate signs of IGC. In contrast, specimens welded at pulse durations of 3 ms and 5 ms show IGC within the WM area. These observations are intensified after a test duration of 40 h, where IGC has penetrated substantial WM areas of specimens welded at pulse durations of 3 ms and 5 ms. Even more so, IGC leads to the detachment and removal of entire grains due to dissolution of the grain boundary vicinity. On the contrary, the etched micrograph of a specimen welded at a pulse duration of 1 ms only exhibits very limited signs of corrosive attack within the WM. It has to be emphasized that for all investigated pulse and test durations, IGC can only be detected within the WM and its fusion line, not within the HAZ. In light of the precipitation behaviour discussed previously, these results suggest that the HAZ sensitization identified during cw-LBW [19, 31] is successfully inhibited through the use of P-LBW. Seemingly, the problematic precipitation conditions are shifted to the WM, which is in good agreement to the analyses of precipitation behaviour presented beforehand. Nonetheless, specimens welded with a pulse duration of 1 ms indicate only very limited signs of IGC.

These findings are further supported by the results of temporally resolved weight loss analysis shown in Fig. 8a. In accordance to the etched micrographs, the mass loss is increased with prolonged test durations as a result of corrosion propagation within the WM.

At all investigated pulse durations, the mass loss increases almost linearly for test intervals of 10 h and 20 h, respectively. However, it can be perceived that the mass loss after a test duration of 40 h does not represent a doubling of the mass loss after 20 h, i.e. the temporally resolved mass loss features a non-linear behaviour. In light of the microscopy images and previous investigations on the IGC behaviour of cw-LBW samples [19], it may be deduced that a regime of internal pitting corrosion is initiated following the primary stages of grain boundary degradation. Since the precipitation of chromium carbides was found to be a spatially selective phenomenon within the WM, the propagation of IGC may be halted at un-sensitized grain boundaries and, thus, limit mass loss. Moreover, the somewhat reduced size of chromium precipitates when using pulse durations of 1 ms in comparison to 5 ms (cf. Figure 6a b) obviously yields reduced chromium depletion in adjacent regions. In addition, the results demonstrate that IGC-based mass loss is minimal for a pulse duration of 1 ms at comparatively long test durations of 20 h and 40 h. A comparison of the weld bead surface after a test duration of 20 h in Fig. 8b gives additional information on the underlying mechanisms. For a pulse duration of 1 ms, IGC is concentrated on the surface of the WM, but does not propagate to the HAZ. In contrast, grain boundaries neighbouring the fusion line are attacked at a pulse duration of 3 ms. Moreover, the grooves evolving from IGC appear deeper and, thus, more significant. Overall, the temporally resolved mass loss is in good agreement to the evolution of residual mechanical strength of laser-cladded AISI 430

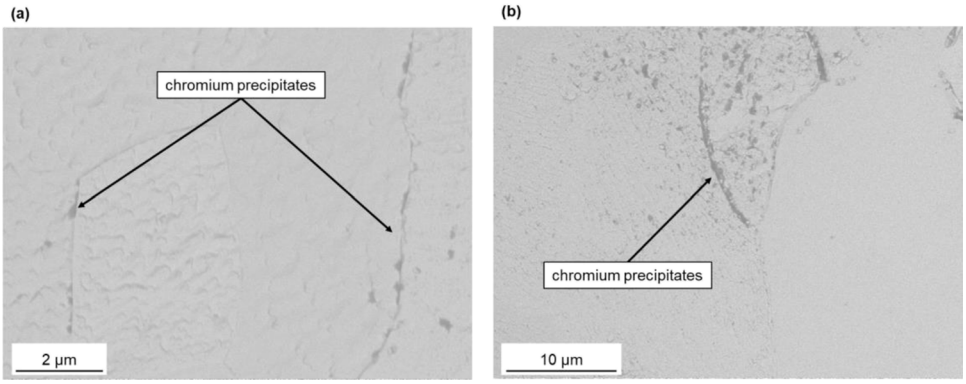

Fig. 6 ESB images visualizing alternating precipitation kinetics within the weld metal of AISI 430 during P-LBW with (a) 1 ms and (b) 5 ms pulse duration

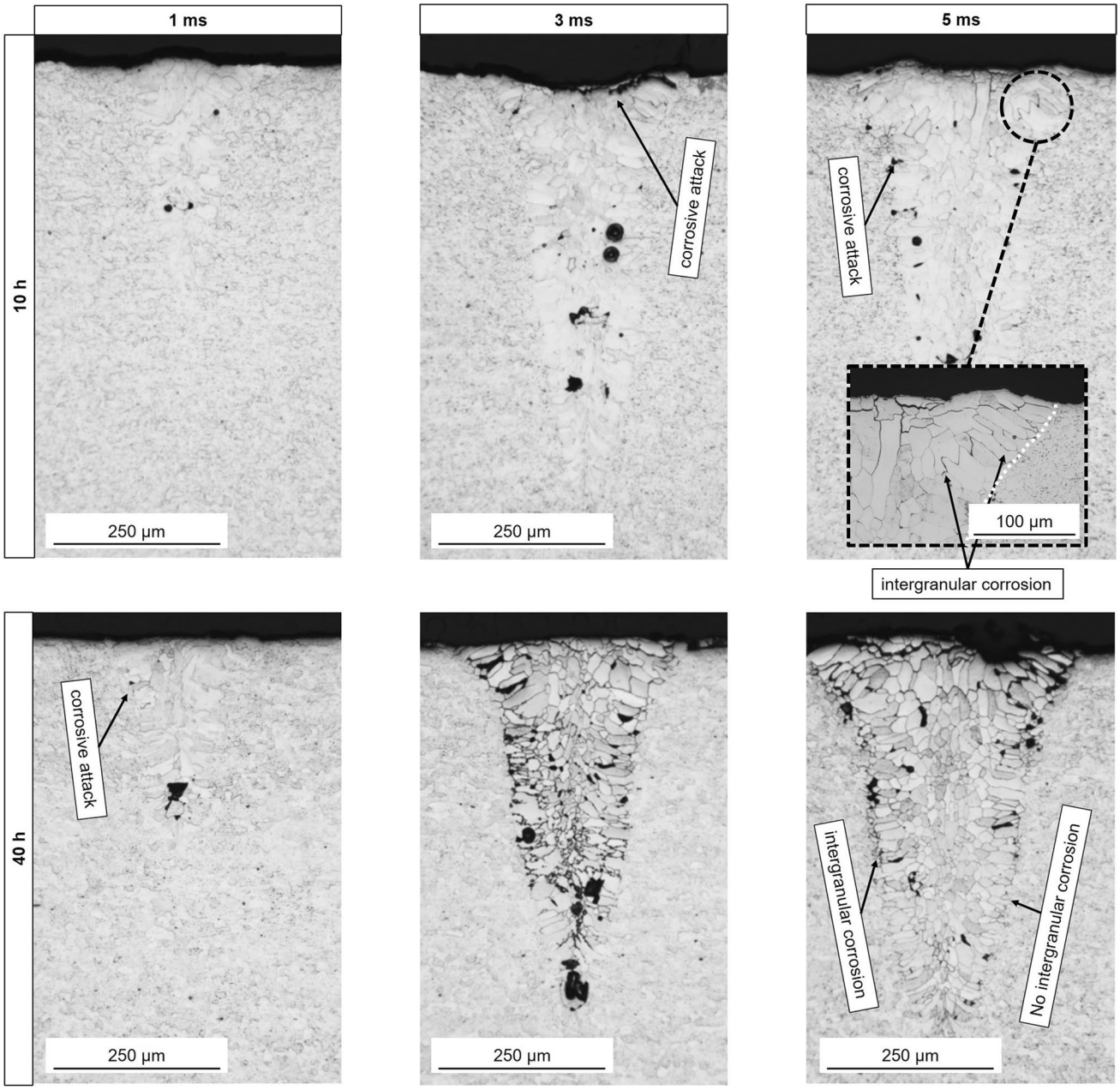

Fig. 7 Etched micrographs of P-LBW AISI 430 using altering pulse durations after corrosion testing

welds which features an approximate exponential decline [33]. In summary, the presented results indicate that the use of comparatively short pulse durations during P-LBW can inhibit chromium carbide precipitation, sensitization and, consequently, IGC within the HAZ due to the inherent thermal gradients and rapid cooling rates, which are obviously amplified in comparison to cw-LBW. Moreover, the use of short pulse durations effectively restricts heat input and, thus, leads to a shortened timeframe for chromium carbide precipitation to occur. As a result, IGC is also substantially limited within the WM.

4 Conclusions

In the present investigation, the effects of varying pulse durations during pulsed laser beam welding with free-form pulse shaping on grain growth and precipitation kinetics of AISI 430 FSS were studied. From the results presented beforehand, a number of conclusions can be drawn:

- Use of a metallurgical pulse shape leads to WM microstructures with pronounced columnar to equiaxed transitions

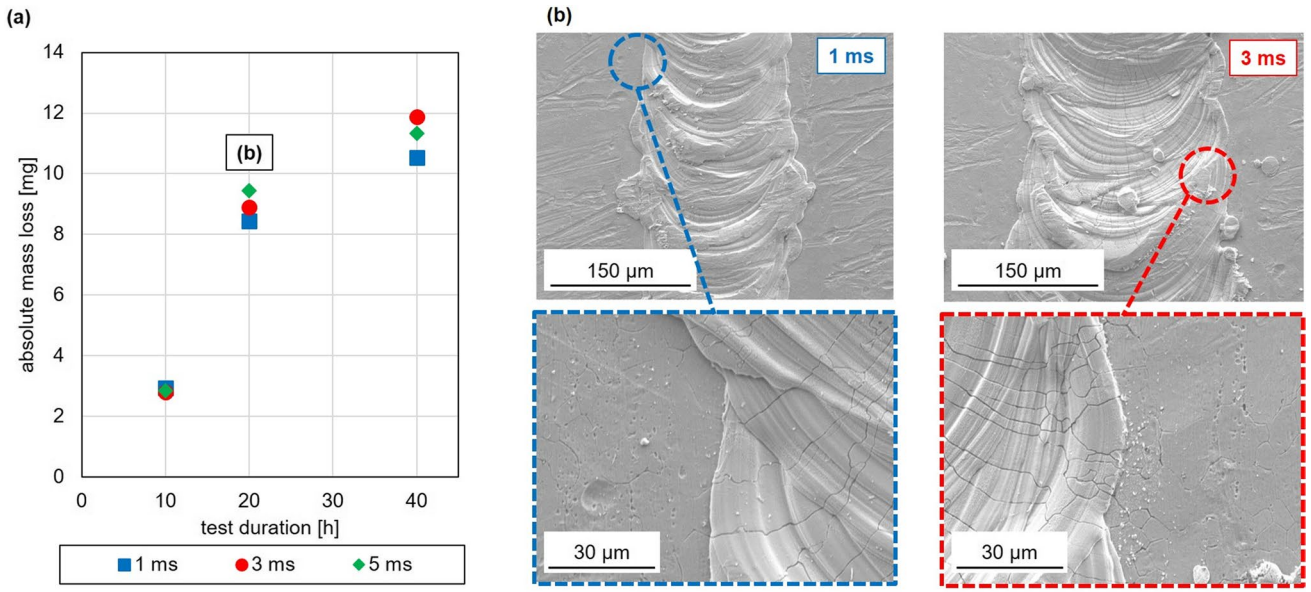

Fig. 8 (a) Absolute mass loss of P-LBW AISI 430 specimens with varying pulse durations in dependence to the test duration. (b) The corresponding SE2 images of the weld bead surface after a test duration of 20 h for pulse durations of 1 ms and 3 ms

- Grain sizes within the equiaxed region are comparable to the unaffected base material
- WM grain size increases with prolonged pulse durations as a result of extended heat input
- Chromium carbide precipitation occurs predominantly within the WM, but is spatially selective
- P-LBW effectively circumvents the precipitation of chromium carbides in the HAZ
- Comparatively long pulse durations yield enlarged chromium carbide precipitation within the WM and, thus, increased intergranular attack

Evidently, the use of P-LBW in combination with free-form pulse shaping enables a tailored heat input which facilitates finer WM grain sizes and limited chromium carbide precipitation. Further research needs to quantify the effects of chromium carbide precipitation along grain boundaries, i.e. by energy-dispersive X-ray spectroscopy, in dependence on pulse durations. Such, it may be viable to develop a process-precipitation model to predict the emergence of IGC.

Acknowledgements The corresponding author thankfully acknowledges the support provided within the framework of "DVS IIW Young Professionals" by the German Welding Society. Furthermore, the authors would like to express their gratitude to Miele & Cie. KG (Gütersloh, Germany) for providing the sheet material used in this study. Parts of the shown results were achieved within the project "Kombiniertes in-situ Laserstrahl-/Laserstrahlauftragschweißen bei nichtrostenden Stählen zum Schutz vor interkristalliner Korrosion" (reference IGF 20.129N), which is supervised by the Forschungsvereinigung Schweißen und verwandte Verfahren e.V. of the German Welding Society and funded by the German Federation of Industrial Research Associations (AiF) by means of the Federal Ministry of Economic Affairs and Climate Action (BMWK) on the basis of a decision by the German Bundestag.

Author contribution Conceptualization: Niklas Sommer; methodology: Niklas Sommer; validation: Niklas Sommer and Stefan Böhm; formal analysis and investigation: Niklas Sommer, Michael Wiegand and Florian Stredak; resources: Stefan Böhm; data curation: Niklas Sommer; writing—original draft preparation: Niklas Sommer; writing—review and editing: Niklas Sommer, Florian Stredak, Michael Wiegand and Stefan Böhm; visualization: Niklas Sommer; supervision: Stefan Böhm; project administration: Niklas Sommer; funding acquisition: Niklas Sommer and Stefan Böhm All authors read and approved the final manuscript.

Funding Open Access funding enabled and organized by Projekt DEAL.

Data availability Data of the present publication cannot be disclosed as they are part of an ongoing investigation.

Declarations

Conflict of interest The authors declare no competing interests.

References

1. Newberg RT, Uhlig HH (1972) Stress corrosion cracking of 18% Cr ferritic stainless steels. J Electrochem Soc 119(8):981. https://doi.org/10.1149/1.2404423
2. A. C. S. Sabioni, A.-M. Huntz, E. C. d. Luz, M. Mantel, and C. Haut, "Comparative study of high temperature oxidation behaviour in AISI 304 and AISI 439 stainless steels," *Mat. Res.*, vol. 6, no. 2, pp. 179–185, 2003, https://doi.org/10.1590/S1516-14392003000200012.
3. International Stainless Steel Forum (2007) The ferritic solution: Properties, advantages, applications; the essential guide to ferritic stainless steels. Brussels
4. Bellezze T, Roventi G, Quaranta A, Fratesi R (2008) Improvement of pitting corrosion resistance of AISI 444 stainless steel to make it a possible substitute for AISI 304L and 316L in hot natural waters. Mater Corros 59(9):727–731. https://doi.org/10.1002/maco.200804112
5. Amuda MOH, Mridha S (2011) An overview of sensitization dynamics in ferritic stainless steel welds. International Journal of Corrosion 2011(4):1–9. https://doi.org/10.1155/2011/305793
6. Berns H, Theisen W (2008) Eisenwerkstoffe: Stahl und Gusseisen, 4th edn. Springer-Verlag, s.l.
7. U. Dilthey, *Schweißtechnische Fertigungsverfahren 2: Verhalten der Werkstoffe beim Schweißen,* 3rd ed. (VDI-Buch). Berlin, Heidelberg: Springer-Verlag Berlin Heidelberg, 2005.
8. Herbsleb G (1968) Untersuchung der Potentialabhängigkeit der interkristallinen Korrosion eines sensibilisierten ferritischen Chromstahls mit rund 17% Cr. Mater Corros 19(3):204–209. https://doi.org/10.1002/maco.19680190304
9. Herbsleb G (1978) Interkristalline Korrosion ferritischer Chromstähle mit rd. 17 Gew.-% Chrom nach Glühen im Temperaturbereich um 500 °C. Mater Corros 29(5):321–325. https://doi.org/10.1002/maco.19780290504
10. Bäumel A (1975) Korrosion in der Wärmeeinflußzone geschweißter chemisch beständiger Stähle und Legierungen und ihre Verhütung. Mater Corros 26(6):433–443. https://doi.org/10.1002/maco.19750260602
11. Pedeferri P (2018) Corrosion Science and Engineering (Engineering Materials). Springer International Publishing, Cham
12. Čihal V (1984) Intergranular corrosion of steels and alloys (Materials science monographs 18). Elsevier, Amsterdam, Oxford, New York, Tokyo
13. Schmidt W, Jarleborg O (1971) Die nichtrostenden ferritischen Stähle mit 17% Chrom. Climax Molybdenum GmbH, Düsseldorf
14. David SA, Vitek JM (1989) Correlation between solidification parameters and weld microstructures. Int Mater Rev 34(1):213–245. https://doi.org/10.1179/imr.1989.34.1.213
15. Evin E, Tomáš M, Výrostek M (2016) Laser-beam welding impact on the deformation properties of stainless steels when used for automotive applications. Acta Mechanica et Automatica 10(3):189–194. https://doi.org/10.1515/ama-2016-0028
16. Schino AD, Kenny JM (2002) Effects of the grain size on the corrosion behavior of refined AISI 304 austenitic stainless steels. J Mater Sci Lett 21(20):1631–1634. https://doi.org/10.1023/A:1020338103964
17. U. Dilthey, *Schweißtechnische Fertigungsverfahren 1: Schweiß- und Schneidtechnologien,* 3rd ed. (SpringerLink Bücher). Berlin, Heidelberg: Springer-Verlag Berlin Heidelberg, 2006.
18. M. Weigl, "Laserstrahlschweißen von Mischverbindungen aus austenitischen und ferritischen korrosionsbeständigen Stahlwerkstoffen," PhD Thesis, FAU, Erlangen-Nürnberg, 2014.
19. Sommer N, Kryukov I, Wolf C, Wiegand M, Kahlmeyer M, Böhm S (2020) On the intergranular corrosion properties of thin ferritic stainless steel sheets welded by fiber-laser. Metals 10(8):1088. https://doi.org/10.3390/met10081088
20. Herbsleb G, Schwenk W (1968) Untersuchungen über die Kornzerfallsanfälligkeit eines unstabilisierten 17%igen Chromstahles und ihre Beseitigung durch Stabilglühen. Mater Corros 19(2):103–113. https://doi.org/10.1002/maco.19680190203
21. Schulze G (2009) Die Metallurgie des Schweißens: Eisenwerkstoffe, Nichteisenmetallische Werkstoffe, 4th edn. Springer-Verlag, s.l.
22. Kiesheyer H, Lennartz G, Brandis H (1976) Korrosionsverhalten hochchromhaltiger, ferritischer, chemisch beständiger Stähle. Mater Corros 27(6):416–424. https://doi.org/10.1002/maco.19760270605
23. E. Wendler-Kalsch and H. Gräfen, *Korrosionsschadenkunde,* 1st ed. (Klassiker der Technik). Berlin: Springer Vieweg, 2012.
24. E. Folkhard, G. Rabensteiner, E. Perteneder, H. Schabereiter, and J. Tösch, *Metallurgie der Schweißung nichtrostender Stähle*. Vienna, s.l.: Springer Vienna, 1984.
25. Park JH, Kim JK, Lee BH, Seo HS, Kim KY (2014) Effect of Zr addition on intergranular corrosion of low-chromium ferritic stainless steel. Scripta Mater 76:77–80. https://doi.org/10.1016/j.scriptamat.2014.01.001
26. Huang X, Wang D, Yang Y (2015) Effect of precipitation on intergranular corrosion resistance of 430 ferritic stainless steel. J Iron Steel Res Int 22(11):1062–1068. https://doi.org/10.1016/S1006-706X(15)30113-8
27. Kim JK, Kim YH, Lee JS, Kim KY (2010) Effect of chromium content on intergranular corrosion and precipitation of Ti-stabilized ferritic stainless steels. Corros Sci 52(5):1847–1852. https://doi.org/10.1016/j.corsci.2010.01.037
28. Kim JK, Kim YH, Lee BH, Kim KY (2011) New findings on intergranular corrosion mechanism of stabilized stainless steels. Electrochim Acta 56(4):1701–1710. https://doi.org/10.1016/j.electacta.2010.08.042
29. Li H, Jiang Z, Feng H, Zhu H, Sun B, Li Z (2013) Corrosion behavior of ferritic stainless steel with 15wt% chromium for the automobile exhaust system. Int J Miner Metall Mater 20(9):850–860. https://doi.org/10.1007/s12613-013-0806-4
30. S. M. Gateman, L. I. Stephens, S. C. Perry, R. Lacasse, R. Schulz, and J. Mauzeroll, "The role of titanium in the initiation of localized corrosion of stainless steel 444," *npj Mater Degrad*, vol. 2, no. 1, p. 1080, 2018, https://doi.org/10.1038/s41529-018-0026-5.
31. N. Sommer, C. Warres, T. Lutz, M. Kahlmeyer, and S. Böhm, "Transmission electron microscopy study on the precipitation behaviors of laser-welded ferritic stainless steels and their implications on intergranular corrosion resistance," *Metals*, vol. 12, no. 1, 2022, https://doi.org/10.3390/met12010086.
32. Sommer N, Stredak F, Böhm S (2021) High-speed laser cladding on thin-sheet-substrates—influence of process parameters on clad geometry and dilution. Coatings 11(8):952. https://doi.org/10.3390/coatings11080952
33. Sommer N, Grimm L, Wolf C, Böhm S (2021) A novel approach to inhibit intergranular corrosion in ferritic stainless steel welds using high-speed laser cladding. Metals 11(12):2039. https://doi.org/10.3390/met11122039
34. Villafuerte JC, Kerr HW, David SA (1995) Mechanisms of equiaxed grain formation in ferritic stainless steel gas tungsten arc welds. Mater Sci Eng, A 194(2):187–191. https://doi.org/10.1016/0921-5093(94)09656-2
35. Durga A et al (2021) Grain refinement in additively manufactured ferritic stainless steel by in situ inoculation using pre-alloyed powder. Scripta Mater 194:113690. https://doi.org/10.1016/j.scriptamat.2020.113690
36. Watanabe T, Shiroki M, Yanagisawa A, Sasaki T (2010) Improvement of mechanical properties of ferritic stainless steel weld metal

by ultrasonic vibration. J Mater Process Technol 210(12):1646–1651. https://doi.org/10.1016/j.jmatprotec.2010.05.015
37. Kou S (2003) Welding metallurgy, 2nd edn. Wiley-Interscience, Hoboken, NJ
38. Reddy GM, Mohandas T (2001) Explorative studies on grain refinement of ferritic stainless steel welds. J Mater Sci Lett 20(8):721–723. https://doi.org/10.1023/A:1010963025259
39. J. Wilden, S. Jahn, P. Kotalí´k, T. P. Neumann, and R. Holtz, "Effects of pulse shape modulation in Nd:YAG laser beam welding on the weld pool flow and solidification," in *ASME 2009 International Manufacturing Science and Engineering Conference, Volume 1*, West Lafayette, Indiana, USA, 2009, pp. 799–805, https://doi.org/10.1115/MSEC2009-84144
40. Kotalík P, Boeck T (2008) Modelling of heat transfer and fluid flow in laser welding. Proc Appl Math Mech 8(1):10623–10624. https://doi.org/10.1002/pamm.200810623
41. Mostaan H and Nematzadeh F (2017) "Micro laser welding of AISI 430 ferritic stainless steel: mechanical properties, magnetic characterization and texture evolution." IJISSI 14(2):1–8. Available: http://journal.issiran.com/article_29647.html
42. Cordovilla F, Tur A, García-Beltrán Á, Diaz M, Angulo I, Ocaña J (2018) Minimization of the thermal impact in the laser welding of dissimilar stainless steels. Metals 8(8):650. https://doi.org/10.3390/met8080650
43. B. Beausir and J.-J. Fundenberger. "Analysis tools for electron and X-ray diffraction: ATEX - software." www.atex-software.eu (accessed Apr. 27, 2022).
44. Determination of resistance to intergranular corrosion of stainless steels — Part 2: Ferritic, austenitic and ferritic-austenitic (duplex) stainless steels — Corrosion test in media containing sulfuric acid (ISO 3651-2 : 1998): German version EN ISO 3651-2 : 1998, DIN EN ISO 3651-2, Deutsches Institut für Normung e. V., Berlin, 1998
45. Xue X, Pereira A, Amorim J, Liao J (2017) Effects of pulsed Nd:YAG laser welding parameters on penetration and microstructure characterization of a DP1000 steel butt joint. Metals 7(8):292. https://doi.org/10.3390/met7080292
46. Dowden JM (ed) (2009) The theory of laser materials processing: heat and mass transfer in modern technology, 1st ed. (Springer series in materials science 119). Dordrecht: Springer
47. Taban E, Deleu E, Dhooge A, Kaluc E (2009) Laser welding of modified 12% Cr stainless steel: strength, fatigue, toughness, microstructure and corrosion properties. Mater Des 30(4):1193–1200. https://doi.org/10.1016/j.matdes.2008.06.030
48. Pekkarinen J, Kujanpää V (2010) The effects of laser welding parameters on the microstructure of ferritic and duplex stainless steels welds. Phys Procedia 5:517–523. https://doi.org/10.1016/j.phpro.2010.08.175
49. Nowell MM, Wright SJ and Carpenter JO (2009) "Differentiating ferrite and martensite in steel microstructures using electron backscatter diffraction," in Materials Science & Technology Conference and Exhibition 2009: Proceedings of a meeting held 25–29 October 2009, Pittsburgh, Pennsylvania. Mater Sci Technol (MS&T), Ed., Red Hook, NY: Curran
50. Wolf C et al (2022) Enhancement of weldability at laser beam welding of 22MnB5 by an entrained ultrasonic wave superposition. Materials 15(14):4800. https://doi.org/10.3390/ma15144800
51. Chan WK, Kwok CT, Lo KH (2020) Mechanical properties and hydrogen embrittlement of laser-surface melted AISI 430 ferritic stainless steel. Coatings 10(2):140. https://doi.org/10.3390/coatings10020140
52. Hennig RG, Trinkle DR, Bouchet J, Srinivasan SG, Albers RC and Wilkins JW (n.d.) "Impurities block the alpha to omega martensitic transformation in titanium." Nat Mater Early Access. https://doi.org/10.1038/nmat1292